



Fluoride-Sulfophosphate/Silica Hybrid Fiber as a Platform for Optically Active Materials

Wei-Chao Wang^{1,2†}, Xu Yang^{1†}, Torsten Wieduwilt³, Markus Alexander Schmidt^{1,3}, Qin-Yuan Zhang² and Lothar Wondraczek^{1*}

¹ Otto Schott Institute of Materials Research, Friedrich Schiller University Jena, Jena, Germany, ² State Key Laboratory of Luminescent Materials and Devices, Guangdong Provincial Key Laboratory of Fiber Laser Materials and Applied Techniques, and Institute of Optical Communication Materials, South China University of Technology, Guangzhou, China, ³ Leibniz Institute of Photonic Technology, Jena, Germany

OPEN ACCESS

Edited by:

Jianrong Qiu,
Zhejiang University, China

Reviewed by:

John Ballato,
Clemson University, United States
Laeticia Petit,
Tampere University of
Technology, Finland

*Correspondence:

Lothar Wondraczek
lothar.wondraczek@uni-jena.de

†These authors have contributed
equally to this work

Specialty section:

This article was submitted to
Glass Science,
a section of the journal
Frontiers in Materials

Received: 11 March 2019

Accepted: 12 June 2019

Published: 12 July 2019

Citation:

Wang W-C, Yang X, Wieduwilt T,
Schmidt MA, Zhang Q-Y and
Wondraczek L (2019)
Fluoride-Sulfophosphate/Silica Hybrid
Fiber as a Platform for Optically Active
Materials. *Front. Mater.* 6:148.
doi: 10.3389/fmats.2019.00148

Pressure-assisted melt filling (PAMF) of pre-fabricated micro-capillaries has been proven an effective way of fabricating hybrid optical fiber (HOF) from unusual combinations of materials. Here, we extend the applicability of PAMF to multi-anionic fluoride-sulfophosphate (FPS) glasses. FPS glasses provide extended transmission windows and high solubility for various transition metal (TM) and rare earth (RE) ion species. Using PAMF for fabricating FPS/silica HOFs can therefore act as a platform for a broad variety of optically active fiber devices. For the present demonstration purposes, we selected Cr³⁺- and Mn²⁺-doped FPS. For both glasses, we demonstrate how the spectral characteristics of the bulk material persist also in the HOF. Using a double-core fiber structure in which waveguiding is conducted in a primary GeO₂-SiO₂ core, mode coupling to the secondary FPS-filled core allows one to exploit the optical activity of the doped FPS glass even when the intrinsic optical loss is high.

Keywords: fluoride-sulfophosphate glass, hybrid fiber, luminescence, pressure-assisted melt filling, optical activity

INTRODUCTION

Fiber lasers are widely used in fields such as materials processing, sensing or, e.g., medical surgery (Jackson, 2012). In order to further extend their ranges of application, fiber materials that operate in different wavelength regimes are continuously being explored, for example, spanning the infrared spectral range for biomedical sensing, or the ultraviolet range for short-wavelength laser output. As an alternative to rare earth (RE) activator ions with mostly *f-f* (or sometimes *f-d*) electronic transitions, transition metal (TM) ions have also attracted great attention, primarily due to the electronic *d-d* transitions that offer significantly enhanced operation bandwidth and, in principle, tunability through adjusting the host material composition (Moncorge, 2017). TM species such as chromium (Yeh et al., 2012), nickel (Samson et al., 2002), or manganese (Ehrt, 2013) in crystalline, glassy, or glass ceramic matrix have been considered for this purpose. As a prominent example, chromium-doped glass fiber was reported for next-generation optical communication systems (Yeh et al., 2012). Efficient laser output was also obtained in the visible to near-infrared spectral range using bismuth-doped glasses as fiber materials (Dianov, 2012). Divalent manganese has drawn attention for its particular combination of tunability in various coordination sites and extended emission lifetime (Da et al., 2010a; Chen et al., 2016; Song et al., 2016).

A major challenge in all these approaches is to find an appropriate combination of matrix material, dopant species, and fiber manufacturing process. Such implementation approaches are currently being used for incorporating various materials into glass fibers, including high-pressure chemical vapor deposition (HPCVD), direct fiber drawing, the molten core method, and melt-in-tube technologies (Ballato and Peacock, 2018). When integrating the multicomponent glasses, crystals, or metals into the silica capillary, however, among other issues, unfavorable combinations of viscosity–temperature behavior and liquidus temperature typically complicate device fabrication. The fabrication of hybrid optical fibers (HOFs) offers some interesting alternatives not only in material processing but also in terms of unconventional combinations of core and cladding materials (Sorin et al., 2007; Schmidt et al., 2016). For example, HOFs may integrate glasses (Jain et al., 2016), crystals (Dragic et al., 2012), semiconductors (Peng et al., 2017), noble-metal nanowires (Tuniz et al., 2017), liquid solutions (Chemnitz et al., 2017), or even gases (Benabid et al., 2002). Current techniques for their fabrication rely mostly on advanced thermal drawing (Cheng et al., 2014; Tuniz et al., 2017) and liquid infiltration of pre-fabricated hollow or microstructured fiber (Da et al., 2010b, 2011; Schmidt et al., 2011; Jain et al., 2016; Tuniz et al., 2017). In particular, for pressure-assisted melt filling (PAMF) of capillary fiber, very high flexibility in terms of material choices and processing conditions was demonstrated. Another key benefit of this approach is that only a small amount of the glass that is to be filled into the capillary is needed. Furthermore, in comparison to other techniques such as rod-in-tube, PAMF avoids extensive pre-processing such as drilling and/or polishing of preforms. Since the fiber core material is encapsulated within the silica capillary, it remains protected from environmental influences, which is important for hygroscopic or toxic glasses acting as the fiber core. In principle, the PAMF technique enables the broadest variety of material combinations. Its major prerequisite and limitation is that the fiber core material needs to provide a low enough viscosity (e.g., <10 Pa·s) at the filling temperature, whereby the filling temperature must be low enough to avoid softening or extensive chemical interaction with the capillary materials (e.g., $<1,200^\circ\text{C}$ for silica). Although both PAMF and HPCVD require processing at elevated pressure, they are inherently different. In the HPCVD, the precursor mixture of raw materials is mechanically pumped into the silica capillary to obtain a high pressure. The deposition is continued until the desired fiber length is fabricated. PAMF, on the other hand, does not involve a gas-phase deposition process. Instead, the fiber core is filled with a pre-conditioned (and homogeneous) glass melt. Using PAMF, glass–glass HOFs have been prepared from combinations of a silica cladding with a chalcogenide (Wang et al., 2015), tellurite (Da et al., 2011), or phosphate (Chemnitz et al., 2016) glass. In particular, the latter holds promise for preparing optically active devices: besides their extended transmission windows in both the UV and IR spectral ranges and distinct dielectric properties, phosphate glasses offer particularly high solubility for RE, TM, or even noble-metal activator species [e.g., Nd^{3+} (Hu et al., 2017), Er^{3+} (Xu et al., 2010), Cr^{3+} (Landry et al., 1967), Mn^{2+} (Ehrt, 2015), Co^{2+} (Griebenow et al., 2017),

or Ag^+ (Thieme et al., 2015)]. As another trait, phosphate glasses exhibit high solubility for secondary anion species such as halides or oxoanions (Le et al., 2017; Wang et al., 2017; Rodrigues et al., 2019). This enables further tailoring of the material's UV-NIR transparency window, its refractive index, partial dispersion, phonon energy and solubility of dopant species, or, e.g., optical non-linearity (Topfer et al., 2000). Such poly-anionic glasses have recently been developed in the fluoride-sulfophosphate (FPS) chemical regime, where extraordinary combinations of highly polarizable sulfate ions, phosphate, and di-phosphate groups and the more localized fluoride ligands were achieved in surprisingly stable glass matrices (Le et al., 2017; Wang et al., 2017). In order to exploit these materials for optical fiber application, we now combine them with PAMF processing of HOFs, fabricating FPS/silica HOFs. In the present work, we explore how the integration of FPS glasses into silica capillaries alters the material's optical properties and how fiber optical waveguides can be obtained. This addresses the potential use of FPS glasses as active media in fiber lasers and other fiber-integrated devices. As a proof of principle, we demonstrate FPS/silica HOFs activated with Mn^{2+} and Cr^{3+} , respectively. These specific TM species have been selected because of their tailorable spectroscopic properties at varying host composition and dopant concentration, and because of their particularly broad emission spectra toward broadband light sources.

EXPERIMENTAL SECTION

Exemplary glass compositions were selected in accordance with a previous analysis of the glass-forming ability of FPS glasses (Le et al., 2017). We chose three different bulk glasses with varying sulfate content, $85(\text{MgF}_2, \text{CaF}_2, \text{SrF}_2, \text{AlF}_3)-(15-x)\text{Sr}(\text{PO}_3)_2-x\text{SrSO}_4$ [mol%, with $x = 5, 10, 15$; denoted FP(15- x)S(x)]. For demonstrating optical activity, additional glasses were prepared from these compositions by doping with 0.05 mol% of Cr_2O_3 and 2 mol% of MnO_2 , respectively. Details on the glass preparation process (including the occurrence of evaporation losses and potential differences between nominal and actual composition) are reported elsewhere (Le et al., 2017). Batches of 100 g were melted in a muffle furnace (using Pt crucibles at $1,000$ – $1,100^\circ\text{C}$) for 2 h, then cooled to 830 – 950°C and poured into a preheated graphite mold. Following this, annealing was conducted for another 2 h at 440 – 510°C , with subsequent cooling to room temperature at a rate of ~ 2 K/min. Differing from this procedure, the compositions with poor glass-forming ability (FP5S10 and FP0S15) were rapidly quenched by pouring the melt onto cold copper plates and immediately pressing with a copper stamp. Subsequent annealing of these samples was done through the same procedure as above. The temperature difference $\Delta T = T_x - T_g$ of the onset temperature of crystallization T_x and the glass transition temperature T_g was taken as a measure of glass stability. Values for FPS10S5, FPS5S10, and FPS0S15 were adopted from a previous study (Wang et al., 2017), i.e., >150 , 133, and 78°C , respectively. Since FPS10S5 exhibits the highest ΔT , it was chosen as the focus composition for the present study, in particular, in the following fiber preparation process.

Hybrid fiber was manufactured using the PAMF method as shown schematically in **Figure 1**. We used the FP10S5 undoped glass, FP10S5:0.05Cr and FP10S5:2Mn, respectively, as the core

materials of different FPS/silica HOFs. Manually drawn strands of these FPS glasses with diameters of $<100\mu\text{m}$ were placed into silica auxiliary capillaries. These were then spliced to the

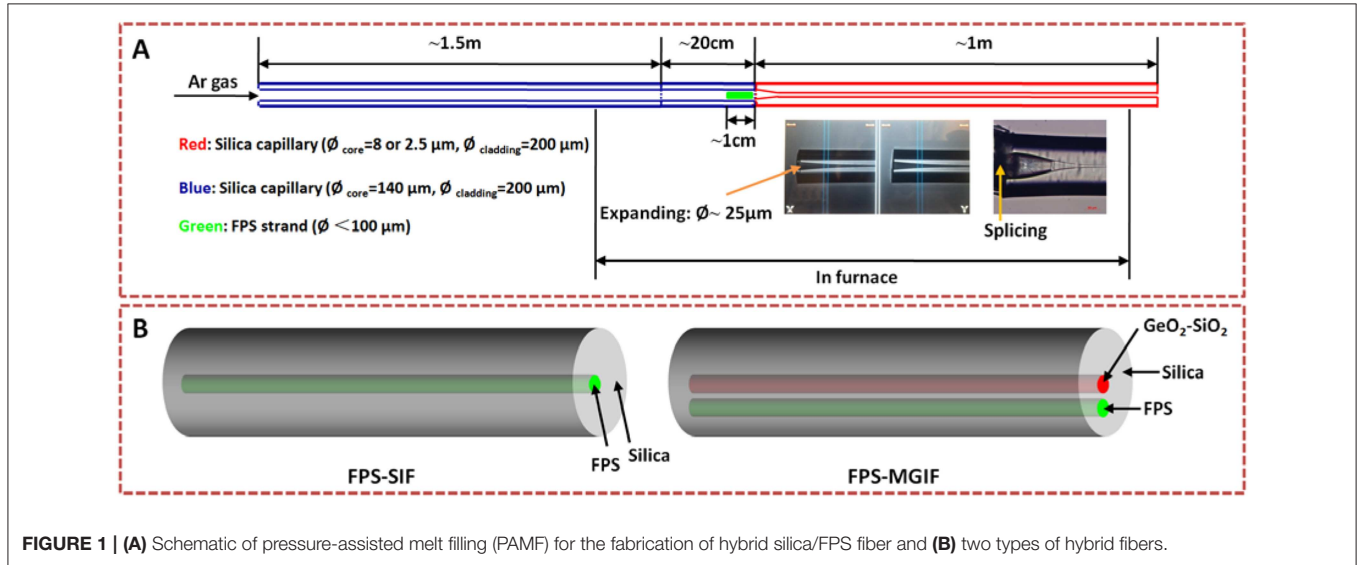


FIGURE 1 | (A) Schematic of pressure-assisted melt filling (PAMF) for the fabrication of hybrid silica/FPS fiber and (B) two types of hybrid fibers.

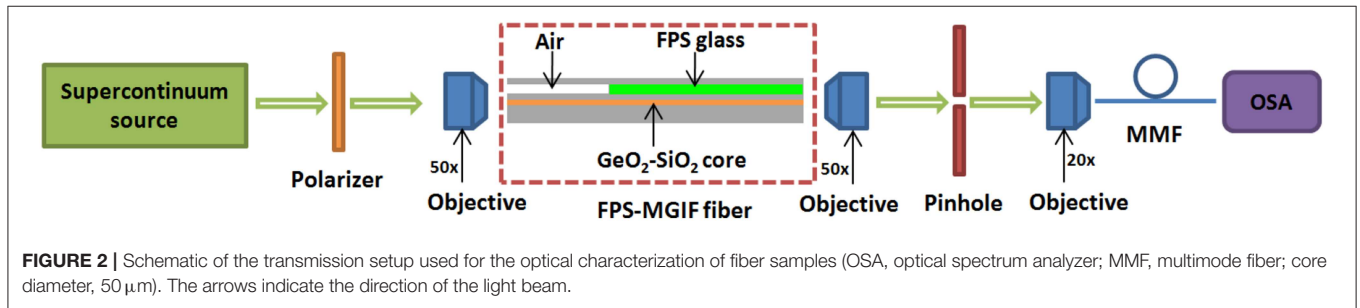


FIGURE 2 | Schematic of the transmission setup used for the optical characterization of fiber samples (OSA, optical spectrum analyzer; MMF, multimode fiber; core diameter, $50\mu\text{m}$). The arrows indicate the direction of the light beam.

TABLE 1 | Reported fiber samples.

Fiber	Core		Cladding		Fiber type
	Composition	Diameter (μm)	Composition	Diameter (μm)	
1	Undoped FP10S5	2.5	SiO_2	200	FPS-SIF
2	Undoped FP10S5	8	SiO_2	200	FPS-SIF
3	FP10S5:0.05Cr	8	SiO_2	200	FPS-SIF
4	FP10S5:2Mn	8	SiO_2	200	FPS-SIF
5	Undoped FP10S5; 89SiO ₂ -11GeO ₂	2.28; 1.9	SiO_2	200	FPS-MGIF

TABLE 2 | Physical properties of silica and FP10S5 used for PAMF.

Glass	Density (g/cm^3)	Refractive index (435.84 nm)	Thermal properties			Mechanical properties		
			Softening temperature($^{\circ}\text{C}$)	Glass transition temperature ($^{\circ}\text{C}$)	Thermal expansion coefficient ($10^{-7}/^{\circ}\text{C}$, 0–300 $^{\circ}\text{C}$)	Elastic modulus(GPa)	Vickers hardness (GPa)	Poisson ratio
Silica	2.2	1.4667	$\sim 1,600$	$\sim 1,120$	5.90	70	8.6–9.8	0.17
FP10S5	3.527	1.4884	478	446.4	14.6	75.4	5.94	0.301

PAMF, pressure-assisted melt filling.

target capillaries and heated on a hot plate so that the FPS filament was melted. Using argon as the transmission medium, the melt was then pressurized so as to infiltrate the target capillary. The filling temperature, filling pressure, and filling time were selected in accordance with previous studies through numerical simulation and experimental optimization (Da et al., 2010b, 2011). For the target capillary, we employed three kinds of silica capillaries that were fabricated by regular fiber drawing from MCVD preforms. These included single-core silica capillaries with channel diameters of 2.5 and 8 μm , respectively, and a modified graded index fiber (MGIF) with a double-core structure. The latter consisted of two parallel channels in which a GeO_2 - SiO_2 -doped core with a diameter of 1.9 μm (GeO_2 peak doping level ~ 11 mol%) and a hollow channel of 2.28 μm are separated by a lateral distance of 3.9 μm (center-to-center). Here, the hollow core was filled with FPS glass. For the single-core capillary with a core diameter of 2.5 μm , PAMF was finally conducted at 750°C and 50 bar for 70 min, while for the single-core capillary with a core diameter of 8 μm , PAMF was conducted at 750°C and 10 bar for 35 min. Both hybrid step index fibers (SIFs) were obtained with typical filling lengths of ~ 10 cm, in

the following referred to as FPS-SIF. For the double-core fiber, the same conditions as for the 2.5- μm capillary were employed (referred to as FPS-MGIF).

UV-Vis-NIR absorption spectra of the bulk glasses were recorded on a double-beam spectrophotometer (Agilent) with a spectral resolution of 1.0 nm. Photoluminescence excitation and emission spectra as well as decay curves were recorded on a high-resolution spectrofluorometer (Horiba Jobin-Yvon), using a continuous-wave 450-W Xe lamp as excitation source and a Hamamatsu R2658P photomultiplier tube for detection. Thermomechanical analyses were conducted on a thermomechanical analyzer (TMA, Netzsch), employing a heating rate of 5 K/min under inert N_2 atmosphere. The elastic properties were characterized by ultrasonic echography on co-planar, optically polished glass plates. The longitudinal and transversal wave velocities were determined with a piezoelectric transducer operating at frequencies of 8–12 MHz (Echometer 1077, Karl Deutsch GmbH & Co KG). For analyzing the filling process, side images were recorded on fiber sections (end, middle) by digital microscopy (Nikon). Furthermore, micro-Raman spectra were also collected on these side views

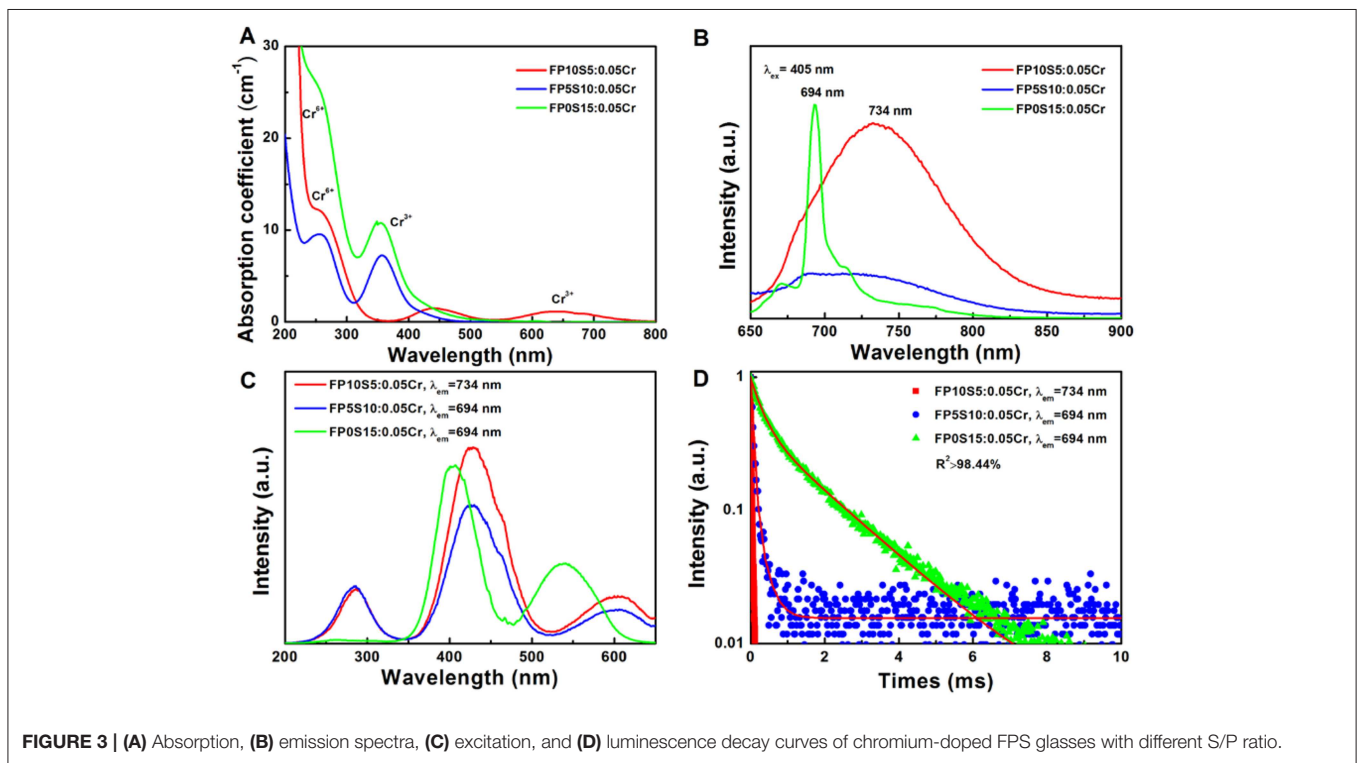


FIGURE 3 | (A) Absorption, (B) emission spectra, (C) excitation, and (D) luminescence decay curves of chromium-doped FPS glasses with different S/P ratio.

TABLE 3 | FPS Cr absorption, photoluminescence spectra, and emission lifetime.

Glass	Absorption (nm)			Emission (nm)	Excitation (nm)			Lifetime (μs)
	Peak 1	Peak 2	Peak 3		Peak 1	Peak 2	Peak 3	
FP10S5:0.05Cr	258	439	640	734	286	428	606	34.5 ± 0.08
FP5S10:0.05Cr	251	357	605	694	285	428	606	74.5 ± 0.34
FP0S15:0.05Cr	258	357	605	694	259	404	539	1070 ± 2.57

(Renishaw) using a 785-nm laser for excitation. For the doped compositions, the local emission spectra of the FPS/silica hybrid fiber were collected with the same Raman microscope, now using a 514-nm laser for excitation. A Raman confocal diameter of about 1 μm and probe powers of 5 and 50 μW were adopted for the bulk glass and fiber, respectively.

Finally, the transmission spectra of FPS/silica hybrid fiber were collected in the visible range using the cut-back method. The transmission setup is illustrated in **Figure 2**. A broadband light source (supercontinuum, 450 nm to 2.4 μm) was coupled into the FPS-MGIF sample using a 50 \times microscope objective after passing through a polarizer oriented along the connection line between the two cores. The transmitted light was out-coupled with a 20 \times objective. An out-coupling objective with relatively small numerical aperture was used to collect only the mode coming from the GeO₂-SiO₂-doped core. The light was then transmitted through a multimode fiber (MMF) to the optical spectrum analyzer (OSA). A pinhole was used to block the light that was guided through the cladding. Higher-order modes from the FPS core with relatively high numerical apertures were not collected. As shown in **Figure 2**, the measured FPS-MGIF sample consists of filled and unfilled sections. There are two purposes to introduce the unfilled section (length of ~ 19 cm): (i) it ensures a good modal overlap at the interface of filled and unfilled sections to guarantee optimal in-coupling, and (ii) it avoids optically induced damage of the FPS end face (Jain et al., 2016). Additionally, the unfilled section was inserted into liquid with a refractive index of 1.52, which further improves the ability to remove the cladding light.

All measurements were performed at room temperature.

The refractive indices of the FPS glasses were determined with a Pulfrich refractometer on samples with a thickness of 5 mm. For quantifying the wavelength dependence, we used the Sellmeier equation (Sardar et al., 2003),

$$n^2 = 1 + \frac{S\lambda^2}{\lambda^2 - \lambda_0^2} \quad (1)$$

where S and λ_0 are empirical fitting parameters.

All the reported fiber samples are listed in **Table 1**. Fibers “1” and “2” were used for microscopic analysis. The reported Raman spectra were collected on Fiber “2” and compared to those of the bulk FP10S5 glass. Fibers “3” and “4” were used for the analysis of the luminescent properties. The attenuation analyses were conducted on Fiber “5.”

RESULTS AND DISCUSSION

Properties of Bulk FPS

The physical properties of silica and FP10S5 glasses as used for PAMF are summarized in **Table 2**. Properties of the silica glass are provided from the manufacturer (Heraeus Suprasil[®]-Family, Spectrosil[®]). From **Table 2**, we find that notable deviations occur in the thermal properties of silica and FPS glasses. The FPS glass has higher density, refractive index, thermal expansion coefficient, elastic modulus, and Poisson ratio than silica. Its

softening temperature, T_g , and hardness are lower. These large deviations result in general incompatibility of the two glasses in classical routes for HOF manufacture, for example, using the rod-in-tube technique. This highlights the most important advantage of the PAMF method, i.e., its wide flexibility in terms of material combinations.

Figure 3 shows the absorption, excitation, emission spectra, and lifetime of chromium-doped FPS bulk glasses with various sulfate contents. The key spectroscopic parameters are summarized in **Table 3**. Obviously, changing glass composition leads to changes in the positions and intensities of the relevant absorption bands of the pertinent Cr species. Chromium exhibits three major absorption peaks originating from Cr³⁺ and Cr⁶⁺ ions (Wang et al., 2017). Due to potential crystallization in the FP0S15:0.05Cr sample, minor amounts of Cr⁴⁺ may also exist in this glass. In the cast FP10S5:0.05Cr glass, there are two broad absorption bands at 439 and 640 nm, mainly originating from the Cr³⁺:⁴A₂ → ⁴T₁ and Cr³⁺:⁴A₂ → ⁴T₂ transitions. In the glass composition with high contents of sulfate (FP0S15:0.05Cr), a very intense absorption band is obtained at ~ 251 nm due to the charge transfer state of Cr⁶⁺. Upon excitation at 405 nm, a broad emission band at around 734 nm is observed in the FP10S5:0.05Cr glass, corresponding to the ⁴T₂ → ⁴A₂ transition of Cr³⁺. With increasing S/P ratio, besides this broad emission band, another overlapping sharper emission band at 694 nm is observed in FP0S15:0.05Cr, originating from the spin-forbidden transition of Cr³⁺:²E → ⁴A₂. This phenomenon implies that higher sulfate content leads to partial crystallization of the FP0S15:0.05Cr sample. By monitoring the emission at 734 nm in the FP10S5:0.05Cr and FP5S10:0.05Cr glasses, a continuous envelope with individual bands at 287, 425, and 600 nm is observed, originating from the ⁴A₂ → ⁴T₁ (⁴P), ⁴A₂ → ⁴T₁ (⁴F), and ⁴A₂ → ⁴T₂ (⁴F) transitions of Cr³⁺. For the FP0S15:0.05Cr glass, a similar excitation spectrum is seen, but with a slight difference of intensity and band positions. The lifetime of the 734-nm emission was 34.5 ± 0.08 μs . For the FP5S10:0.05Cr and FP0S15:0.05Cr samples, the lifetimes of the emission band at 694 nm reached about 74.5 ± 0.34 and 1,070 ± 2.57 μs , respectively. The much longer lifetime of 1,070 ± 2.57 μs in FP0S15:Cr glass is taken as a further result of the presence of a crystalline phase.

For the Mn²⁺-doped glasses, the absorption, emission, excitation, and luminescence decay curves are provided in **Figure 4**. The key spectroscopic parameters are also summarized in **Table 4**. The broadband absorption peak at ~ 488 nm and its two shoulder peaks at 405 and 607 nm are assigned to the electronic transitions of ⁵E_g → ⁵T_{2g} of Mn³⁺ (3d⁴ configuration, with the characteristic purple coloration), and ⁶A₁(⁶S) → ⁴A₁(⁴G), ⁴E_g(⁴G), and ⁶A₁(⁶S) → ⁴T₂(⁴G) of Mn²⁺ (3d⁵ configuration), respectively (Reddy et al., 2016). With increasing S/P ratio, the ultraviolet cutoff sideband of the Mn-doped glass shows a distinct blue shift. Upon excitation at 405 nm, a broad emission band occurs at around 590 nm (FP10S5:2Mn), corresponding to the ⁶T₁(⁴G) → ⁶A₁(⁶S) transition of Mn²⁺. The emission wavelength shows a slightly blue shift (from 590 to 576 nm), and the emission intensity becomes weaker

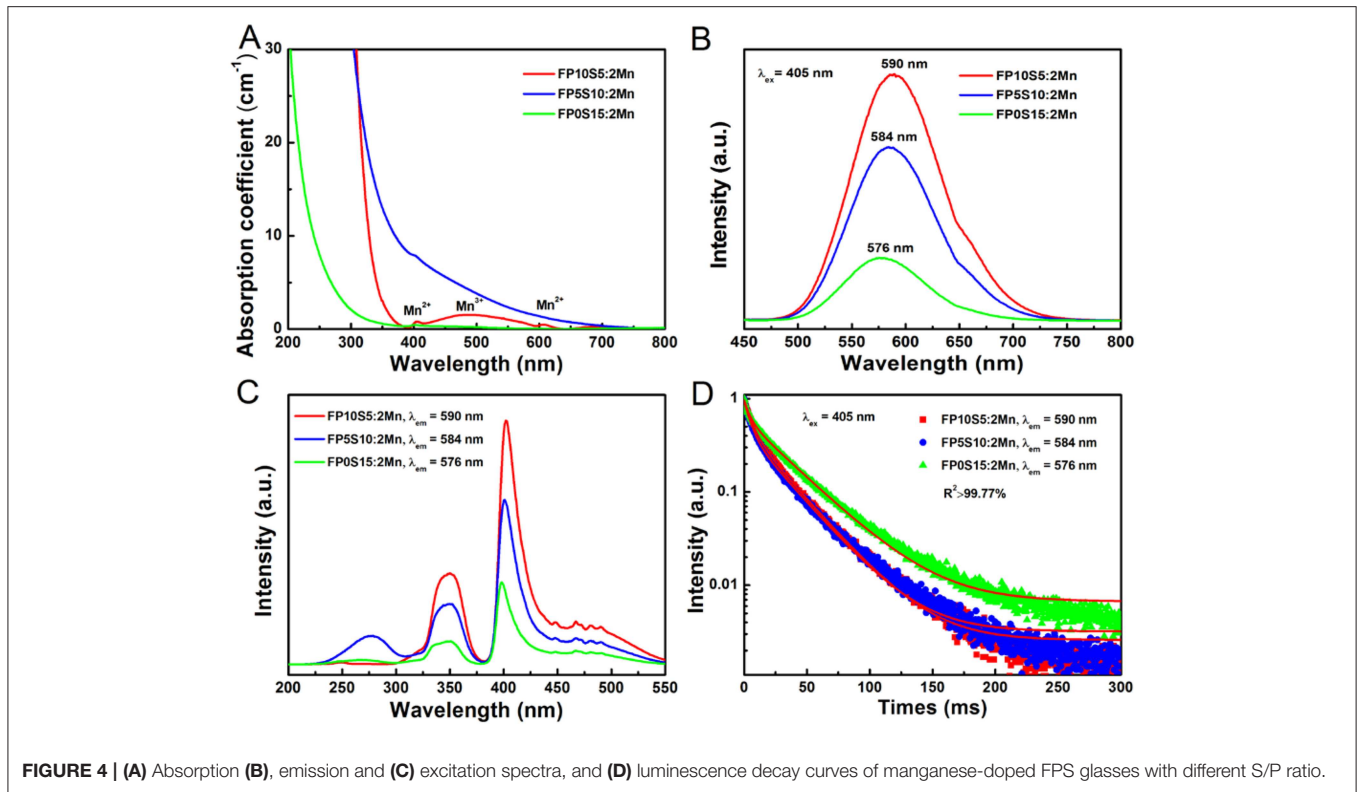


FIGURE 4 | (A) Absorption (B), emission and (C) excitation spectra, and (D) luminescence decay curves of manganese-doped FPS glasses with different S/P ratio.

TABLE 4 | FPS Mn absorption, photoluminescence spectra, and decay time.

Glass	Absorption (nm)			Emission (nm)	Excitation	Lifetime (ms)
	Peak 1	Peak 2	Peak 3	Peak 1	(nm)	
FP10S5:2Mn	405	488	607	590	402	19 ± 0.02
FP5S10:2Mn	405	–	–	584	401	21 ± 0.05
FP0S15:2Mn	405	–	–	576	398	28 ± 0.06

with increasing sulfate content. This emission wavelength is significantly shorter than the one that was previously observed in fluoride-free sulfophosphate glasses (Da et al., 2010a; Möncke et al., 2014). Without going into detail at this point, we further note that the emission band is asymmetric with an overlapping feature at around 648 nm, similar to observations on Mn-doped borophosphate glasses (Ehrt, 2009). The strong compositional dependence of the emission properties of Mn^{2+} results from the underlying $d-d$ transitions and their interactions with the ligand field. In the present case, Gaussian deconvolution of the emission spectra reveals the presence of two distinct components at around 580 and 630 nm. The former band is found to blue-shift (from 590 to 576 nm) with increasing S/P ratio. At the same time, its width decreases from 95 to 87 nm full width at half maximum (FWHM). The notable variation in Mn^{2+} -related photoluminescence from glasses is typically related to variations in Mn^{2+} coordination between tetrahedral (green emission, high optical basicity) and octahedral (orange-red, low optical basicity) (Ehrt, 2009). We find similar features on the

excitation spectra that correspond to the emissions at 590, 584, and 576 nm (see Figure 4C): all excitation spectra are composed of peaks at ~250, 350, 402, and 480 nm, corresponding to the transitions from ${}^6A_1({}^6S)$ to ${}^4T_1({}^4P)$, ${}^4T_2({}^4D)$, $[{}^4A_1({}^4G), {}^4E({}^4G)]$, and ${}^4T_1({}^4G)$, respectively. The dominant excitation peak is the one at ~402 nm, which is in agreement with the absorption spectra shown in Figure 4A. There is a slight blue shift of this band from 402 to 398 nm, and a red shift of the UV band from 250 to 278 nm with increasing sulfate content. The decay curves of the Mn^{2+} -related emission exhibit a non-exponential character with average lifetimes of $\sim 19 \pm 0.02$, 21 ± 0.05 , and 28 ± 0.06 ms, respectively, for increasing sulfate content. The lifetime of the Mn^{2+} -related emission slightly differs from that of other glasses, for example, Mn^{2+} -doped phosphate (14–21 ms) (Möncke et al., 2011; Zhang et al., 2013) or sulfophosphate glasses (14.0–16.8 ms) (Da et al., 2010a), but it is significantly longer than that of borate (7 ms) (Ehrt, 2013) or aluminosilicate (~5–6 ms) (Lakshminarayana and Wondraczek, 2011) glasses.

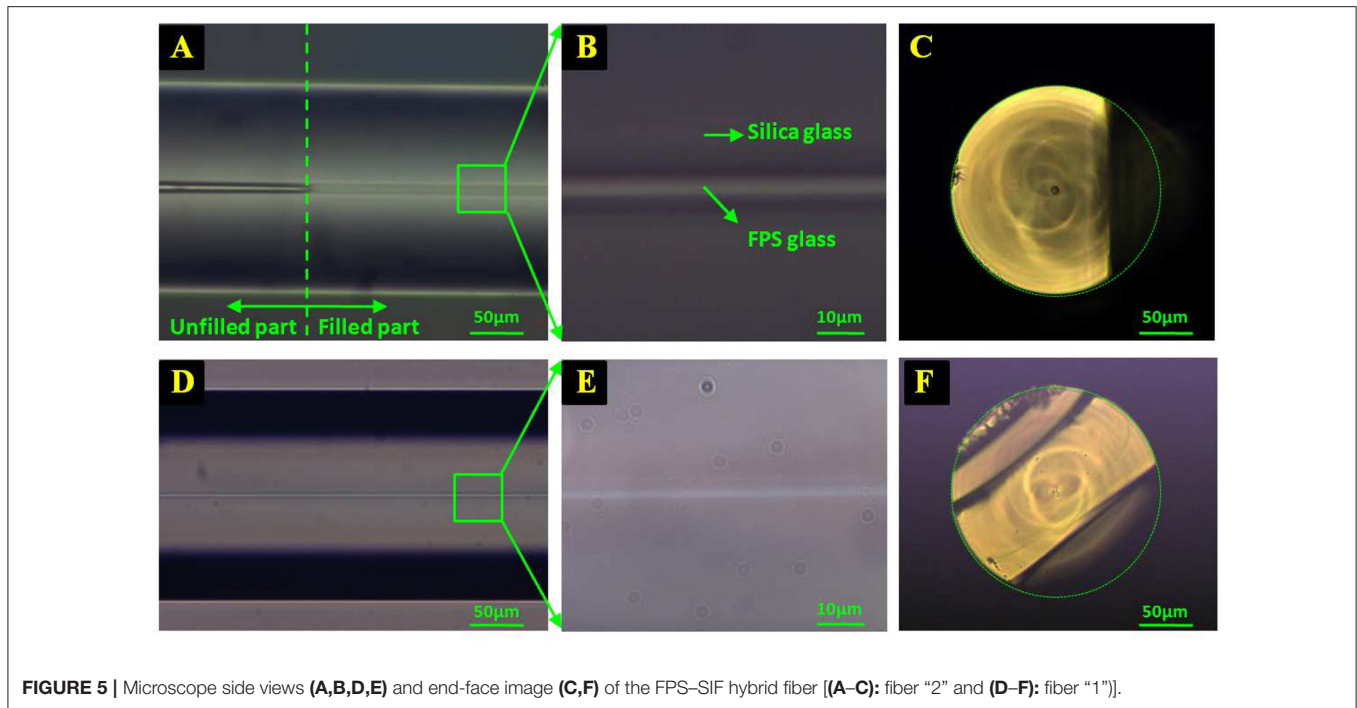


FIGURE 5 | Microscope side views (A,B,D,E) and end-face image (C,F) of the FPS-SIF hybrid fiber [(A-C): fiber “2” and (D-F): fiber “1”].

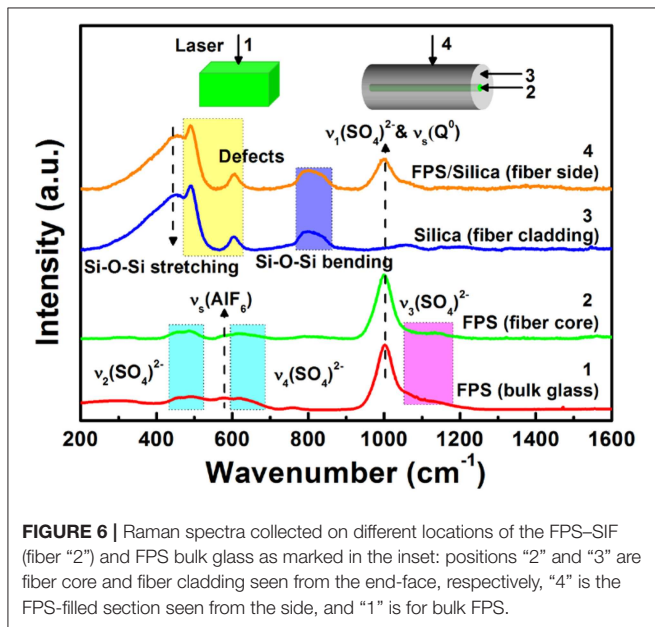


FIGURE 6 | Raman spectra collected on different locations of the FPS-SIF (fiber “2”) and FPS bulk glass as marked in the inset: positions “2” and “3” are fiber core and fiber cladding seen from the end-face, respectively, “4” is the FPS-filled section seen from the side, and “1” is for bulk FPS.

FPS/Silica Hybrid Fibers

Side views and end-face photographs of typical FPS/silica hybrid fibers with different core diameters are provided in Figure 5 (shown for undoped FPS-SIF). Figure 5A shows the boundary region between the FPS-filled and the unfilled section of a capillary with an inner diameter of $8\mu\text{m}$. A zoom at the filled core regions (Figures 5B,E) reveals that the FPS glass is in physical contact with the silica capillary alongside the full length of the filled sections in both fibers and that there is no

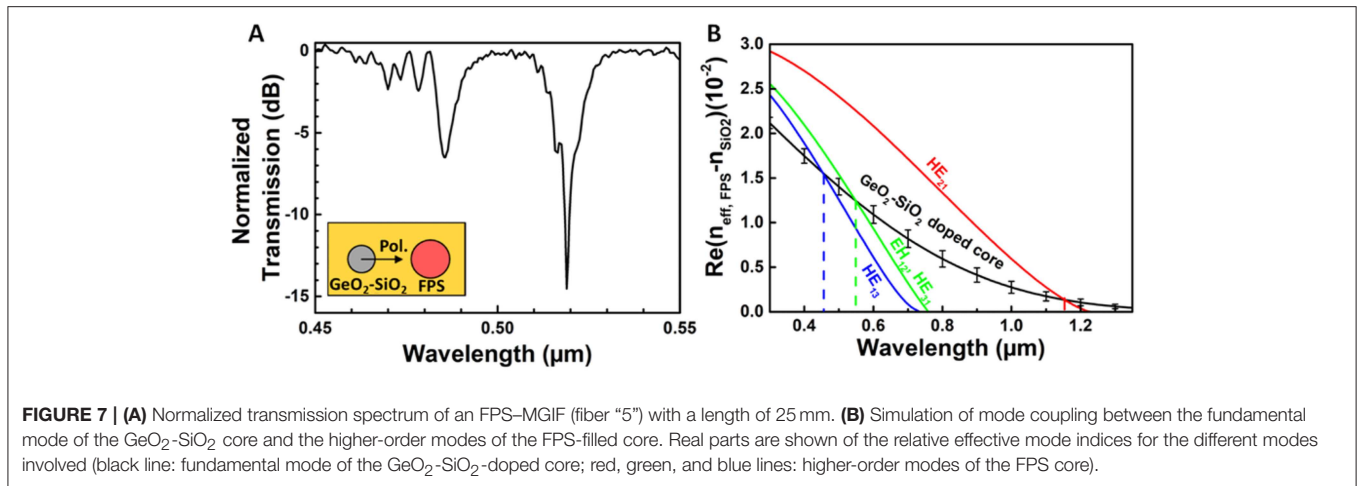
delamination, porosity, or particle precipitation at least for this present observation.

Raman Spectroscopy

Raman spectra of the filled section and of the cladding of FPS-SIF (fiber “2”) are given in Figure 6. The spectra were collected on four different locations as marked in the inset of Figure 6, i.e., on the surface of the bulk glass (1), on the fiber core (2), and on the fiber cladding (3) as seen on the fiber end face, and on the side view of the FPS section in the hybrid fiber (4). Spectra “1” and “2” basically correspond to FPS glass, and “3” is of silica alone, whereas “4” contains convoluted information from silica and FPS. The Raman spectra of the bulk FPS glass and of the fiber core are in very good agreement with previous structural analyses of similar FPS materials (Le et al., 2017), allowing for a clear assignment of the characteristic vibrations of $\nu_1(\text{SO}_4)^{2-}$ and $\nu_s(\text{Q}^0)$ ($1,000\text{ cm}^{-1}$), $\nu_2(\text{SO}_4)^{2-}$ (470 cm^{-1}), and $\nu_4(\text{SO}_4)^{2-}$ (624 cm^{-1}). The silica cladding “3” shows its typical Si-O-Si stretching (445 cm^{-1}) and defect modes (491 and 605 cm^{-1}), together with the Si-O-Si bending mode (800 cm^{-1}) (Henderson et al., 2009). Together, all of these observations are taken as direct evidence for the efficiency of melt infiltration without notable chemical interaction between the FPS melt and the capillary walls. Noteworthy at this point, we did not observe any hints for silica dissolution such as Si-O-P stretching vibrations ($1,145\text{ cm}^{-1}$) (Shibata et al., 1981) or traces of crystal precipitation.

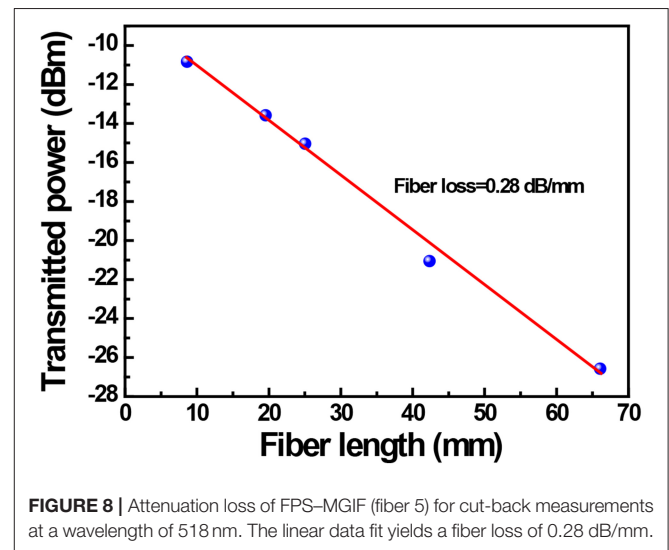
Attenuation Measurement

Optical attenuation analysis provides qualitative information on the potential use cases of HOF devices as fiber optical waveguides. As a first step and without targeting minimal loss figures, we



intend to prove optical guidance. Secondly, also in the absence of direct transmission, mode interaction in multi-core fiber can be of interest (Schmidt et al., 2009). For this reason, we considered the double-core fiber in which guidance occurs by total reflection in the GeO₂-SiO₂-doped region, and the (active) FPS region is exploited through mode coupling. As a directional mode coupler, the electromagnetic energy of the dual-core FPS-MGIF waveguide system is exchanged periodically along the longitudinal direction, which makes it an efficient narrowband optical fiber-integrated notch filter. The initial length of the FPS-MGIF (fiber “5”), which was used for attenuation analysis, was 68 mm. Five cut-back measurements were carried out. **Figure 7A** shows an example transmission spectrum with a FPS-MGIF length of 25 mm. The spectrum was normalized to a reference transmission spectrum of an unfilled MGIF. In this case, the polarization direction of incident light is parallel to the connection line of the two cores. The spectra show a series of peaks that result from modes coupling between the fundamental mode of the GeO₂-SiO₂ core and higher-order modes of the FPS core. The normalized attenuation is 15 dB with an FWHM bandwidth of 8 nm at the deepest dip located at 518 nm.

As described above, the MGIF consists of the GeO₂-SiO₂ core and the FPS core, which offers a large core-cladding index difference. By analyzing the dispersion characteristics of double-core MGIF, we can understand the operation of such hybrid fiber as a mode coupler. **Figure 7B** shows a simulation result of mode coupling in the FPS-MGIF. Two sharp transmission dips are observed in both polarization states with dip center wavelengths at 486 and 519 nm. These dips are associated with a matching of higher-order FPS core modes with the fundamental mode of the GeO₂-SiO₂ core. At these positions, the effective indices of the FPS modes cross the dispersion of the GeO₂-SiO₂ core mode and then the minimum transmission is observed. The maximum resonance extinction is about 15 dB with a full width half maximum bandwidth of only 2 nm for the resonance at 519 nm. The dispersion of the fundamental mode HE₁₁ of the GeO₂-SiO₂ core and the dispersions of the modes of the FPS were calculated by a mode solver (ATSOS). For the calculation of existing modes



in the FPS core, the refractive indices of doped and undoped silica dioxide were applied. Here, a higher refractive index for the FPS glass was used instead of the measured refractive index of the bulk glass (increased by $\Delta n = 0.007$) mainly because of the following two reasons: (i) The molten FPS glass was pressed by the argon gas into the small hollow capillary, which was moved out of the furnace promptly after filling process. Therefore, the residual stress likely increased the density of the material which results in a somewhat larger refractive index (Yablon, 2004). (ii) The accuracy of the ellipsometry for the measurement of refractive index is ± 0.005 . Thus, it is reasonable to increase the refractive index by a same magnitude. The relative effective mode index between the effective index of the FPS modes and the refractive index of pure silica ($n_{eff,FPS} - n_{SiO_2}$) are plotted to rescale the y-axis for better illustration. The couplings occur at those wavelengths where the curves of the higher FPS modes (HE₁₃, HE₃₁, EH₁₂) intersect with the curve of fundamental mode of the GeO₂-SiO₂ core. The fundamental mode (HE₁₁) of the FPS core does not show a cross-point with the GeO₂-SiO₂ mode in

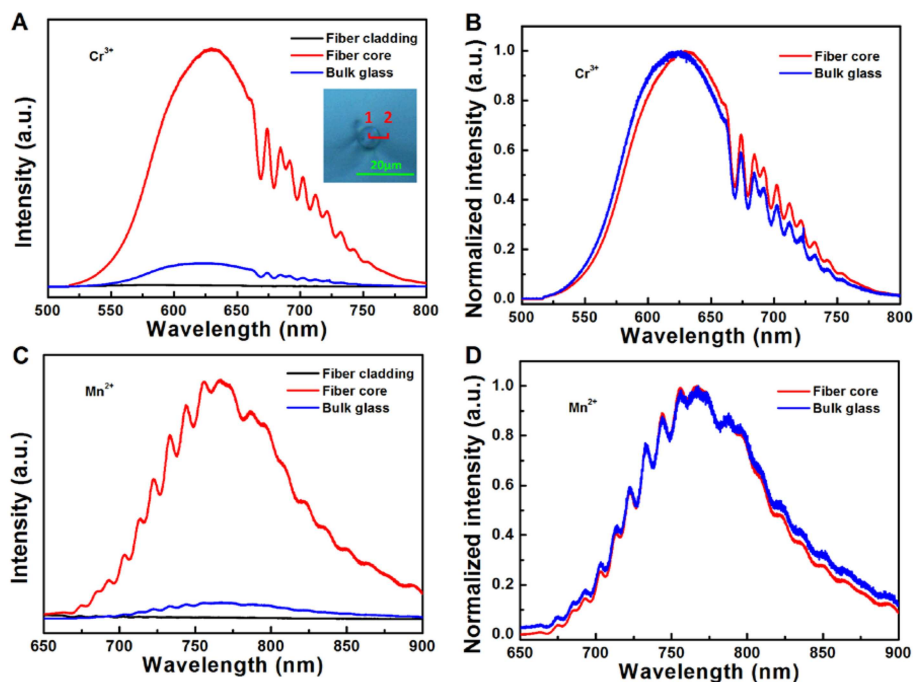


FIGURE 9 | (A) Local emission spectra and **(B)** normalized emission spectra of the FPS/silica hybrid fiber doped with Cr³⁺ (fiber “3”) and comparison to bulk FPS glass counterpart. **(C)** Local emission spectra and **(D)** normalized emission spectra of the FPS/silica hybrid fiber doped with Mn²⁺ (fiber “4”) and comparison to bulk FPS glass counterpart. The inset shows the fiber core/cladding boundary region; positions “1” and “2” are the fiber core and cladding (located from the core/cladding boundary $\sim 3 \mu\text{m}$), respectively.

the observed spectral range. As seen in **Figure 7B**, the simulation reveals the first coupling in the infrared range; the second and third couplings are in the visible wavelength range. In the VIS range, the simulated resonance wavelengths are also at 486 and 519 nm, which are consistent with the results in the transmission spectra. The simulation results have good matching with respect to the experimental result, indicating that the refractive index of the FPS strand within the capillary is a little higher than the bulk sample.

The attenuation of the FPS–MGIF (fiber 5) at a wavelength of 518 nm was determined based on the five different cut backs (**Figure 8**). Using linear regression, the attenuation loss was calculated at 0.28 dB/mm. The higher fiber loss originates primarily from the intentional dopants, but potentially also from impurities in the raw materials. In addition, due to the mismatch between the thermal expansion coefficient of FPS glass and silica, interface roughness may be another factor. Although the fiber loss is high, it is already lower than previous reports on other PAMF-derived HOFs. For example, in a similar metaphosphate/silica hybrid fiber, such system’s potential for supercontinuum generation was demonstrated even for a fiber loss of ~ 0.35 dB/mm (Chemnitz et al., 2016). Further reduction of fiber loss may be envisioned for optimized processing and enhanced purity of raw materials. From the present demonstration study, we conclude at this point that the FPS–MGIF system can act as an efficient and narrow bandwidth fiber-integrated notch filter.

Local Emission Spectra of the FPS/Silica Hybrid Fiber

The local emission spectra of the FPS/silica SIF hybrid fiber doped with Cr³⁺ (fiber “3”) and Mn²⁺ (fiber “4”) as well as a comparison with FPS bulk glass measured using a Raman microscope with a 514-nm laser excitation are given in **Figure 9**. We find intense luminescence at 767 and 630 nm in the Mn²⁺- and Cr³⁺-doped fiber core (position “1,” see the inset of **Figure 9**), respectively. The emission characteristics are similar to those of the bulk glasses when the spectra are normalized, with a slight red shift at the higher excitation wavelength. In the undoped cladding region, no emission is observed (position “2”). Other Mn²⁺- and Cr³⁺-doped glass fibers have been investigated recently. For example, Mn²⁺-doped gallate glass and glass fiber were prepared by Lv et al. (2018). They observed a broad emission band at 635 nm and a more narrow emission at 506 nm in the Mn²⁺-doped gallate glass and glass ceramic, respectively, which resulted in red and green emission color. As another example, Fang et al. obtained an intense emission band ranging from 600 to 800 nm in a Cr³⁺-doped glass ceramic fiber upon excitation at 532 nm (Fang et al., 2015). The much narrower emission bands than our results are because of the strong crystal field of the glass ceramic matrix.

CONCLUSIONS

We presented PAMF for poly-anionic FPS glasses, fabricating FPS/silica HOF as a platform for a broad variety of optically active

fiber devices. For demonstration purposes, we chose Cr^{3+} - and Mn^{2+} -doped FPS, on which we have shown how the spectral characteristics of the bulk material persist also in the hybrid fiber. Using a double-core fiber structure in which waveguiding is conducted in the primary GeO_2 - SiO_2 core with mode coupling to the secondary FPS-filled core allows for exploiting the optical activity of the material even at high intrinsic loss.

DATA AVAILABILITY

The datasets generated for this study are available on request to the corresponding author.

AUTHOR CONTRIBUTIONS

LW and MS conceived the present project. W-CW carried out the FPS glass and strand fabrication and was responsible

for the majority of physical characterization (including UV-Vis absorption, Raman, photoluminescence, and photoluminescence excitation spectroscopy). XY and TW conducted the PAMF experiments and analyzed the obtained HOF devices. All authors participated in data evaluation, discussion, and interpretation.

FUNDING

This work was funded by the German Science Foundation (DFG) through grants no. WO1220/9-2, WO1220/15-1, and SCHM2655/10-1. W-CW gratefully acknowledges the Chinese Scholarship Council (CSC) for personal support.

ACKNOWLEDGMENTS

We thank our colleagues at OSIM for help with sample preparation and data acquisition.

REFERENCES

- Ballato, J., and Peacock, A. C. (2018). Perspective: molten core optical fiber fabrication—a route to new materials and applications. *APL Photonics* 3:120903. doi: 10.1063/1.5067337
- Benabid, F., Knight, J. C., Antonopoulos, G., and Russell, P. S. J. (2002). Stimulated Raman scattering in hydrogen-filled hollow-core photonic crystal fiber. *Science* 298, 399–402. doi: 10.1126/science.1076408
- Chemnitz, M., Gebhardt, M., Gaida, C., Stutzki, F., Kobelke, J., Limpert, J., et al. (2017). Hybrid soliton dynamics in liquid-core fibres. *Nat. Commun.* 8, 1–11. doi: 10.1038/s41467-017-00033-5
- Chemnitz, M., Wei, J. X., Jain, C., Rodrigues, B. P., Wieduwilt, T., Kobelke, J., et al. (2016). Octave-spanning supercontinuum generation in hybrid silver metaphosphate/silica step-index fibers. *Opt. Lett.* 41, 3519–3522. doi: 10.1364/OL.41.003519
- Chen, Z. T., Song, E. H., Wu, M., Zhou, B., and Zhang, Q. Y. (2016). Exchange coupled Mn–Mn pair: an approach for super-broadband 1380 nm emission in α -MnS. *Appl. Phys. Lett.* 109:191907. doi: 10.1063/1.4967452
- Cheng, T. L., Gao, W. Q., Kawashima, H., Deng, D., Liao, M., Matsumoto, M., et al. (2014). Widely tunable second-harmonic generation in a chalcogenide–tellurite hybrid optical fiber. *Opt. Lett.* 39, 2145–2147. doi: 10.1364/OL.39.002145
- Da, N., Enany, A. A., Granzow, N., Schmidt, M. A., Russell, P. S., and Wondraczek, L. (2011). Interfacial reactions between tellurite melts and silica during the production of microstructured optical devices. *J. Non Cryst. Solids* 357, 1558–1563. doi: 10.1016/j.jnoncrysol.2010.12.032
- Da, N., Peng, M., Krolikowski, S., and Wondraczek, L. (2010a). Intense red photoluminescence from Mn^{2+} -doped (Na^+ ; Zn^{2+}) sulfophosphate glasses and glass ceramics as LED converters. *Opt. Express* 18, 2549–2557. doi: 10.1364/OE.18.002549
- Da, N., Wondraczek, L., Schmidt, M. A., Granzow, N., and Russell, P. S. J. (2010b). High index-contrast all-solid photonic crystal fibers by pressure-assisted melt infiltration of silica matrices. *J. Non Cryst. Solids* 356, 1829–1836. doi: 10.1016/j.jnoncrysol.2010.07.002
- Dianov, E. M. (2012). Bismuth-doped optical fibers: a challenging active medium for near-IR lasers and optical amplifiers. *Light Sci. Appl.* 1, 1–7. doi: 10.1038/lsa.2012.12
- Dragic, P., Hawkins, T., Foy, P., Morris, S., and Ballato, J. (2012). Sapphire-derived all-glass optical fibres. *Nat. Photonics* 6, 627–633. doi: 10.1038/nphoton.2012.182
- Ehrt, D. (2009). Photoluminescence in glasses and glass ceramics. *IOP Conf. Ser. Mater. Sci. Eng.* 2:012001. doi: 10.1088/1757-899X/2/1/012001
- Ehrt, D. (2013). Zinc and manganese borate glasses—phase separation, crystallisation, photoluminescence and structure. *Phys. Chem. Glasses B* 54, 65–75.
- Ehrt, D. (2015). Phosphate and fluoride phosphate optical glasses—properties, structure and applications. *Phys. Chem. Glasses B* 56, 217–234. doi: 10.13036/17533562.56.6.217
- Fang, Z. J., Zheng, S. P., Peng, W. C., Zhang, H., Ma, Z. J., Zhou, S. F., et al. (2015). Fabrication and characterization of glass-ceramic fiber-containing Cr^{3+} -doped ZnAl_2O_4 nanocrystals. *J. Am. Ceram. Soc.* 98, 2772–2775. doi: 10.1111/jace.13716
- Griebenow, K., Hoppe, U., Möncke, D., Kamitsos, E. I., and Wondraczek, L. (2017). Transition-metal incorporation and Co-Sr/Mn-Sr mixed-modifier effect in metaphosphate glasses. *J. Non Cryst. Solids* 460, 136–145. doi: 10.1016/j.jnoncrysol.2017.01.022
- Henderson, G. S., Neuville, D. R., Cochain, B., and Cormier, L. (2009). The structure of GeO_2 - SiO_2 glasses and melts: a Raman spectroscopy study. *J. Non Cryst. Solids* 355, 468–474. doi: 10.1016/j.jnoncrysol.2009.01.024
- Hu, L. L., He, D. B., Chen, H. Y., Wang, X., Meng, T., Wen, L., et al. (2017). Research and development of neodymium phosphate laser glass for high power laser application. *Opt. Mater.* 63, 213–220. doi: 10.1016/j.optmat.2016.11.052
- Jackson, S. D. (2012). Towards high-power mid-infrared emission from a fibre laser. *Nat. Photonics* 6, 423–431. doi: 10.1038/nphoton.2012.149
- Jain, C., Rodrigues, B. P., Wieduwilt, T., Kobelke, J., Wondraczek, L., and Schmidt, M. A. (2016). Silver metaphosphate glass wires inside silica fibers—a new approach for hybrid optical fibers. *Opt. Express* 24, 3258–3267. doi: 10.1364/OE.24.003258
- Lakshminarayana, G., and Wondraczek, L. (2011). Photoluminescence and energy transfer in $\text{Tb}^{3+}/\text{Mn}^{2+}$ co-doped ZnAl_2O_4 glass ceramics. *J. Solid State Chem.* 184, 1931–1938. doi: 10.1016/j.jssc.2011.05.059
- Landry, R. J., Fournier, J. T., and Young, C. G. (1967). Electron spin resonance and optical absorption studies of Cr^{3+} in a phosphate glass. *J. Chem. Phys.* 46, 1285–1290. doi: 10.1063/1.1840846
- Le, Q. H., Palenta, T., Benzine, O., Griebenow, K., Limbach, R., Kamitsos, E. I., et al. (2017). Formation, structure and properties of fluoro-sulfo-phosphate poly-anionic glasses. *J. Non Cryst. Solids* 477, 58–72. doi: 10.1016/j.jnoncrysol.2017.09.043
- Lv, S. C., Shanmugavelu, B., Wang, Y. P., Mao, Q. N., Zhao, Y. J., Yu, Y. Z., et al. (2018). Transition metal doped smart glass with pressure and temperature sensitive luminescence. *Adv. Opt. Mater.* 6:1800881. doi: 10.1002/adom.201800881
- Möncke, D., Kamitsos, E. I., Herrmann, A., Ehrt, D., and Friedrich, M. (2011). Bonding and ion-ion interactions of Mn^{2+} ions in fluoride-phosphate and boro-silicate glasses probed by EPR and fluorescence spectroscopy. *J. Non Cryst. Solids* 357, 2542–2551. doi: 10.1016/j.jnoncrysol.2011.02.017
- Möncke, D., Sirotkin, S., Stavrou, E., Kamitsos, E. I., and Wondraczek, L. (2014). Partitioning and structural role of Mn and Fe ions in ionic sulfophosphate glasses. *J. Chem. Phys.* 141:224509. doi: 10.1063/1.4903191

- Moncorge, R. (2017). Laser materials based on transition metal ions. *Opt. Mater.* 63, 105–117. doi: 10.1016/j.optmat.2016.05.060
- Peng, S., Tang, G. W., Huang, K. M., Qian, Q., Chen, D. D., Zhang, Q. Y., et al. (2017). Crystalline selenium core optical fibers with low optical loss. *Opt. Mater. Express* 7, 1804–1812. doi: 10.1364/OME.7.001804
- Reddy, C. P., Naresh, V., and Reddy, K. T. R. (2016). Li₂O-LiF-ZnF₂-B₂O₃-P₂O₅: MnO glasses—thermal, structural, optical and luminescence characteristics. *Opt. Mater.* 51, 154–161. doi: 10.1016/j.optmat.2015.11.035
- Rodrigues, B. P., Ebdorff-Heidepriem, H., and Wondraczek, L. (2019). Decoupling mobility and charge carrier concentration in AgR-AgPO₃ glasses (R = Cl, Br, I). *Solid State Ion.* 334, 99–104. doi: 10.1016/j.ssi.2019.02.009
- Samson, B. N., Pinckney, L. R., Wang, J., Beall, G. H., and Borrelli, N. F. (2002). Nickel-doped nanocrystalline glass-ceramic fiber. *Opt. Lett.* 27, 1309–1311. doi: 10.1364/OL.27.001309
- Sardar, D. K., Gruber, J. B., Zandi, B., Hutchinson, J. A., and Trussell, C. W. (2003). Judd-Ofelt analysis of the Er³⁺(4f¹¹) absorption intensities in phosphate glass: Er³⁺, Yb³⁺. *J. Appl. Phys.* 93, 2041–2046. doi: 10.1063/1.1536738
- Schmidt, M. A., Argyros, A., and Sorin, F. (2016). Hybrid optical fibers—An innovative platform for in-fiber photonic devices. *Adv. Opt. Mater.* 4, 13–36. doi: 10.1002/adom.201500319
- Schmidt, M. A., Granzow, N., Da, N., Peng, M., Wondraczek, L., Russell, P., et al. (2009). All-solid band-gap guiding in tellurite-filled silica photonic crystal fibers. *Opt. Lett.* 34, 1946–1948. doi: 10.1364/OL.34.001946
- Schmidt, M. A., Wondraczek, L., Lee, H. W., Granzow, N., Da, N., Russell, P., et al. (2011). Complex Faraday rotation in microstructured magneto-optical fiber waveguides. *Adv. Mater.* 23, 2681–2688. doi: 10.1002/adma.201100364
- Shibata, N., Horigudhi, M., and Eda, H. (1981). Raman-spectra of binary high-silica glasses and fibers containing GeO₂, P₂O₅ and B₂O₃. *J. Non Cryst. Solids* 45, 115–126. doi: 10.1016/0022-3093(81)90096-X
- Song, E. H., Chen, Z. T., Wu, M., Ding, S., Ye, S., Zhou, S. F., et al. (2016). Room-temperature wavelength-tunable single-band upconversion luminescence from Yb³⁺/Mn²⁺ codoped fluoride perovskites ABF₃. *Adv. Opt. Mater.* 4, 798–806. doi: 10.1002/adom.201500732
- Sorin, F., Abouraddy, A. F., Orf, N., Shapira, O., Viens, J., Arnold, J., et al. (2007). Multimaterial photodetecting fibers: a geometric and structural study. *Adv. Mater.* 19, 3872–3877. doi: 10.1002/adma.200700177
- Suprasil®. Heraeus. Available online at: <https://www.heraeus.com>
- Thieme, A., Möncke, D., Limbach, R., Fuhrmann, S., Kamitsos, E. I., Wondraczek, L. (2015). Structure and properties of alkali and silver sulfophosphate glasses. *J. Non-Cryst. Solids* 410, 142–150.
- Topfer, T., Hein, J., Philipps, J., Ehrhart, D., and Sauerbrey, R. (2000). Tailoring the nonlinear refractive index of fluoride-phosphate glasses for laser applications. *Appl. Phys. B* 71, 203–206. doi: 10.1007/s003400000240
- Tuniz, A., Chemnitz, M., Dellith, J., Weidlich, S., and Schmidt, M. A. (2017). Hybrid-mode-assisted long-distance excitation of short-range surface plasmons in a nanotip-enhanced step-index fiber. *Nano Lett.* 17, 631–637. doi: 10.1021/acs.nanolett.6b03373
- Wang, S. Y., Jain, C., Wondraczek, L., Wondraczek, K., Kobelke, J., Troles, J., et al. (2015). Non-Newtonian flow of an ultralow-melting chalcogenide liquid in strongly confined geometry. *Appl. Phys. Lett.* 106, 201908. doi: 10.1063/1.4921708
- Wang, W. C., Le, Q. H., Zhang, Q. Y., and Wondraczek, L. (2017). Fluoride-sulfophosphate glasses as hosts for broadband optical amplification through transition metal activators. *J. Mater. Chem. C* 5, 7969–7976. doi: 10.1039/C7TC01853C
- Xu, S. H., Yang, Z. M., Liu, T., Zhang, W. N., Feng, Z. M., Zhang, Q. Y., et al. (2010). An efficient compact 300 mW narrow-linewidth single frequency fiber laser at 1.5 μm. *Opt. Express* 18, 1249–1254. doi: 10.1364/OE.18.001249
- Yablon, A. D. (2004). Optical and mechanical effects of frozen-in stresses and strains in optical fibers. *IEEE J. Sel. Top. Quantum Electron.* 10, 300–311. doi: 10.1109/JSTQE.2004.826570
- Yeh, S. M., Huang, S. L., Chiu, Y. J., Taga, H., Huang, P. L., Huang, Y. C., et al. (2012). Broadband chromium-doped fiber amplifiers for next-generation optical communication systems. *J. Lightwave Technol.* 30, 921–927. doi: 10.1109/JLT.2012.2182758
- Zhang, W. J., Gao, G., Möncke, D., Winterstein-Beckmann, A., Zhang, Q. Y., Peng, M., et al. (2013). Mn²⁺-sensitized near-IR emission in Nd³⁺-activated Sr,Mn- metaphosphate glasses. *J. Non Cryst. Solids* 380, 60–64. doi: 10.1016/j.jnoncrysol.2013.08.004

Conflict of Interest Statement: The authors declare that the research was conducted in the absence of any commercial or financial relationships that could be construed as a potential conflict of interest.

Copyright © 2019 Wang, Yang, Wieduwilt, Schmidt, Zhang and Wondraczek. This is an open-access article distributed under the terms of the Creative Commons Attribution License (CC BY). The use, distribution or reproduction in other forums is permitted, provided the original author(s) and the copyright owner(s) are credited and that the original publication in this journal is cited, in accordance with accepted academic practice. No use, distribution or reproduction is permitted which does not comply with these terms.